https://doi.org/10.3311/PPch.44080

Periodica Polytechnica Chemical Engineering

Analysis of Wettability and Contact Angle Hysteresis on a Thermally Treated Low Free Energy Surface

Vishwajeet Kumar[1], Jyoti Kumar[1], Abhik Majumder[1*]

[1] Department of Mechanical Engineering, National Institute of Technology Agartala, Tripura 799046, India
[*] Corresponding author, e-mail: abhik.me@faculty.nita.ac.in

Received: 23 March 2026, Accepted: 24 July 2026, Published online: 13 September 2026

Abstract

The biomimetic replication of the lotus leaf to create hierarchical surface morphology has attracted significant research interest due to its potential applications in self-cleaning, anti-corrosion, anti-fouling, and anti-icing surfaces. Several attempts have been made to create such structure using metal-fatty acid combination. However, zinc myristate (ZnMTA) surfaces have not been fully explored, despite their relevance and promise in surface engineering. In this study, a superhydrophobic coating was fabricated on a copper substrate through the electrochemical deposition of zinc, followed by thermal annealing and surface modification using myristic acid (MTA). The electrodeposition and annealing processes generated a hierarchical micro–nano surface morphology, whereas surface modification led to the formation of a low-surface-energy ZnMTA layer. Scanning electron microscopy revealed micro-scale clusters decorated with nano-petal structures, producing void spaces capable of trapping air. Quantitative image analysis indicated a void fraction of 86.7 ± 5.4%, which is conducive to the formation of a Cassie–Baxter-type wetting regime. As a result, the coating exhibited excellent water repellency, with a water contact angle of 156° ± 0.8°, contact angle hysteresis of 5°, and roll-off angle or sliding angle of 4°. High-speed imaging of droplet impact further demonstrated droplet rebound with a contact time of 28 ms and a spreading factor of β = 2.33, indicating weak liquid–solid adhesion forces. The combination of hierarchical roughness and low surface energy renders the developed coating promising for applications requiring durable water-repellent surfaces.

Keywords

superhydrophobic coating, zinc myristate (ZnMTA), hierarchical micro–nano structure, electrochemical deposition, Cassie–Baxter wetting, droplet rebound, contact angle hysteresis (CAH)

1 Introduction

The study of wettability on surfaces has been explored rigorously in recent decades due to the promising aspect of its practical implications [1–4]. The wettability of a surface is quantified by the water contact angle θ (WCA). It is the angle formed at the three-phase contact line between the liquid–vapor interface and the solid surface. Based on the contact angle the surfaces have been classified into four categories (Fig. 1) [5]. Surfaces are typically categorized as superhydrophilic ($\theta < 10°$), hydrophilic ($10° \leq \theta < 90°$), hydrophobic ($90° \leq \theta < 150°$), and superhydrophobic ($\theta \geq 150°$). One of the extremes of this spectrum is superhydrophobicity, in which a surface shows superior anti-wetting properties with a WCA greater than 150° [6]. Naturally occurring substances, such as lotus leaf, are known to show such excellent anti-wetting property with low sliding angle (SA), commonly known as "lotus leaf

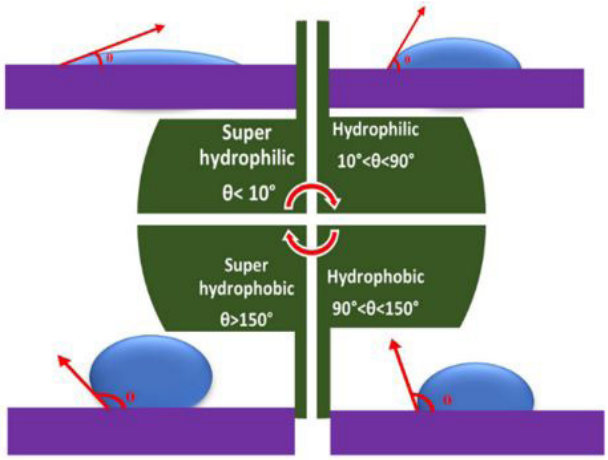

Fig. 1 Classification of solid surfaces based on water contact angle (WCA) showing superhydrophilic, hydrophilic, hydrophobic, and superhydrophobic regimes

Cite this article as: Kumar, V., Kumar, J., Majumder, A. "Analysis of Wettability and Contact Angle Hysteresis on a Thermally Treated Low Free Energy Surface", Periodica Polytechnica Chemical Engineering, 2026. https://doi.org/10.3311/PPch.44080

effect" [7]. The study of such naturally occurring surfaces revealed that the combined effect and physical and chemical characteristics of the surface impart such superior anti wetting properties. At the physical level, the surface should have binary roughness, whereas at the chemical level, it should have low surface energy [8, 9].

For rough and textured surfaces, apparent wettability is often interpreted using the Wenzel and Cassie–Baxter models, which describe complete wetting and composite solid–air wetting states, respectively [10, 11]. Although the WCA provides information on surface hydrophobicity, it does not fully characterize droplet mobility and adhesion. Therefore, additional parameters, such as the contact angle hysteresis (CAH) and roll-off or SA, are frequently employed (Fig. 2). CAH, defined as the difference between the advancing and receding contact angles, is closely associated with contact line pinning and droplet adhesion. Low CAH and SA facilitate the movement of the three-phase contact line of the droplet on the surface; hence, a superhydrophobic surface (WCA > 150°) with low hysteresis and roll-off angle exhibits low adhesion between the droplet and the surface, and the drop can easily roll off the surface, which is pivotal in applications such as self-cleaning. Whereas the a superhydrophobic surface (WCA > 150°) with high CAH and SA show high adhesion between droplet and surface due to pinning of droplet pivotal in applications like separation process and directional liquid transport [12]. Lotus leaves and rose petals both exhibit contact angle in excess of 150°, but the CAH on a lotus leaf is <5°; whereas, rose petal show a high CAH of 105° [12, 13]. Lotus leaves exhibit low CAH because they maintain a stable Cassie–Baxter state with trapped air, resulting in a minimal contact area and low adhesion. In contrast, rose petals exhibit high hysteresis because of a composite Cassie–Baxter wetting state, where partial liquid penetration increases the solid–liquid contact and promotes strong pinning.

Superhydrophobic coatings have been extensively developed on a wide range of substrates, including metals, polymers, glass, and ceramics, depending on the intended application [14–16]. Among these, metallic substrates have attracted significant attention due to their widespread industrial use and susceptibility to corrosion [16–18]. Copper and its alloys, being among the most widely used metals in applications ranging from heat exchangers and electrical instruments to marine and medical equipment, have been the focus of considerable research on superhydrophobic coatings and their corresponding wettability characteristics [19]. In this context, long-chain fatty acids, such as myristic acid (MTA), stearic acid (STA), and palmitic acid (PA), are commonly employed for surface modification, as their extended hydrocarbon chains effectively reduce surface energy, making them highly suitable for achieving superhydrophobic behaviour. Liu et al. [20] studied the cerium myristate coating on a copper substrate and found a WCA of 161.7°and a CAH of 3°. Yuan et al. [21] formed a fluoropolymer film on a through graft polymerization on copper substrate and found a WCA of 159° and corrosion efficiency of 95.3%. Zhi Chen et al. [9] studied the electrodeposited coating of lanthanum chloride and MTA on copper. A high WCA of 165° with a SA of 2° was observed. Fan et al. [22] studied the superhydrophobic coating through electrodeposition on both cathode and anode with copper as substrate. They used STA as surface modifier and found the contact angle on both the electrodes were greater than 150°, while cathode showed a SA of 4° the anode showed a SA of 6.2°. Yang et al. [23] coated the copper substrate with nickel and MTA through electrodeposition and found a WCA of 160.3 ± 1.5° with SA of 3.0 ± 0.5°. Xi et al. [24] studied the WCA and the SA on electrodeposited copper substrate. They used aqueous 0.08 M $CuSO_4$ and 0.06 M H_2SO_4 as an electrolyte. The study of surface morphology with scanning electron microscopy (SEM) revealed a lotus like morphology and a WCA and SA of 153.5° and 7.9° respectively. Han Jie et al. [25] studied the coating on brass substrate though combination of etching and heat treatment approach followed by low surface energy modification of STA.

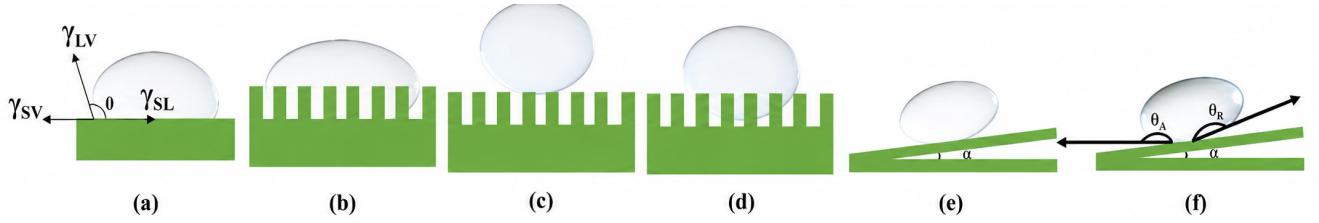

Fig. 2 Schematic illustration of different wetting states and droplet dynamics on solid surfaces: (a) Young's wetting state on an ideal smooth surface; (b) Wenzel state where the liquid fully penetrates the surface roughness; (c) Cassie–Baxter state where the droplet rests on surface asperities with trapped air pockets; (d) Cassie–Wenzel transition illustrating partial liquid penetration into surface structures; (e) roll-off angle depicting droplet motion on an inclined surface; and (f) contact angle hysteresis showing advancing and receding contact angles.

They found a high WCA of 153.6° with excellent anticorrosive property. Some researchers have also developed superhydrophobic coating on other substrates like Lee et al. [26] studied the superhydrophobic coating of Cu-Ni composite electrodeposition on a silicon wafer which shows a WCA of 158° ± 1° with a SA of 10°. Li et al. [27] studied the coating of Cu-Zn coating on steel substrate without any further surface modification. Interestingly after 60 days of storage in air the coating turned superhydrophobic with WCA 154.73° and SA of 6.5. Mamgain et al. [28] have fabricated Cu–Al superhydrophobic coating fabricated on steel via electrodeposition followed by STA modification, achieving a WCA of 152° and corrosion protection efficiency of 98%. The enhanced performance was attributed to the hierarchical nano-flower morphology and reduced electrolyte–surface contact. Tran et al. [29] fabricated a superhydrophobic aluminium surface by combining laser texturing, boiling-water-induced pseudo-boehmite nanostructures, and silicone oil modification, achieving a corrosion protection efficiency of up to 99.4% along with excellent environmental stability and water-repellent performance. Wang et al. [30] developed a facile and scalable spray-coating approach using HDTMS-modified diatomite and epoxy resin to fabricate superhydrophobic coatings on magnesium alloys, achieving a WCA of 157°, corrosion protection efficiency of 99.8%, and excellent anti-icing, chemical stability, and mechanical robustness. Tan et al. [31] developed a superhydrophobic Co/Ag composite coating through one-step electrodeposition, exhibiting excellent water repellency (WCA = 163.8°), superior corrosion protection, mechanical robustness, and anti-biofouling properties for marine applications.

Despite extensive research on superhydrophobic coatings for metallic substrates, most studies primarily report the WCA as the principal metric for evaluating surface wettability and deals with the application aspect of the coating like anti-corrosion, anti-icing, self-cleaning etc. While the contact angle (CA) provides information about the static wetting behaviour and the degree of hydrophobicity of a surface, CAH reflects the difference between the advancing and receding contact angles and is closely associated with droplet adhesion and pinning on the surface [32, 33]. Similarly, SA represents the inclination angle at which a droplet begins to move, providing insight into droplet mobility on textured surfaces [14]. A limited number of studies have systematically investigated the combined influence of these parameters together with surface morphology and chemical modification, particularly in coatings modified with long-chain fatty acids, such as MTA. The absence of such integrated analyses creates an important gap in understanding how hierarchical surface structures and surface chemistry collectively influence droplet dynamics and wetting regimes, which is crucial for optimizing functional superhydrophobic coatings for practical applications. Addressing this limitation is therefore essential for advancing both the fundamental understanding of wetting mechanisms and the development of surfaces with controlled droplet mobility for applications such as self-cleaning, anti-corrosion, and condensation management. Furthermore, to the best of our knowledge, the dynamic wetting characteristics of electrodeposited and myristic-acid-modified superhydrophobic coatings, particularly droplet rebound behaviour, contact time, and spreading dynamics, have not been systematically correlated with CAH, SA, and surface void fraction. The present work deals with the integrated evaluation of static wettability, droplet adhesion, and impact dynamics in conjunction with detailed morphological, chemical, and void fraction analyses, thereby providing a comprehensive understanding of the relationship between surface structure, surface chemistry, and droplet mobility.

In the present study, a facile electrochemical deposition approach combined with MTA modification is employed to fabricate a superhydrophobic coating on a copper substrate (Fig. 3). The influence of MTA concentration on wettability is systematically investigated through a comprehensive evaluation of the WCA, CAH, SA, and droplet impact dynamics, together with detailed morphological and chemical characterization. The optimized coating exhibited a high-WCA of 156° ± 0.8°, low CAH of 5°, and a SA of 4°, demonstrating excellent water repellency and low droplet adhesion. High-speed imaging further revealed rapid droplet rebound with a contact time of 28 ms and a spreading factor of $\beta = 2.33$, indicating efficient energy restitution and weak liquid–solid interaction. These results highlight that the enhanced wetting performance arises from the synergistic effect of a hierarchical micro–nano surface architecture and reduced surface energy associated with zinc myristate (ZnMTA) formation, which collectively promote air entrapment and stabilization of the Cassie–Baxter wetting regime. The present study thus provides a deeper understanding of the relationship between surface structure, surface chemistry, and droplet dynamics, offering valuable insights for the design of advanced superhydrophobic coatings.

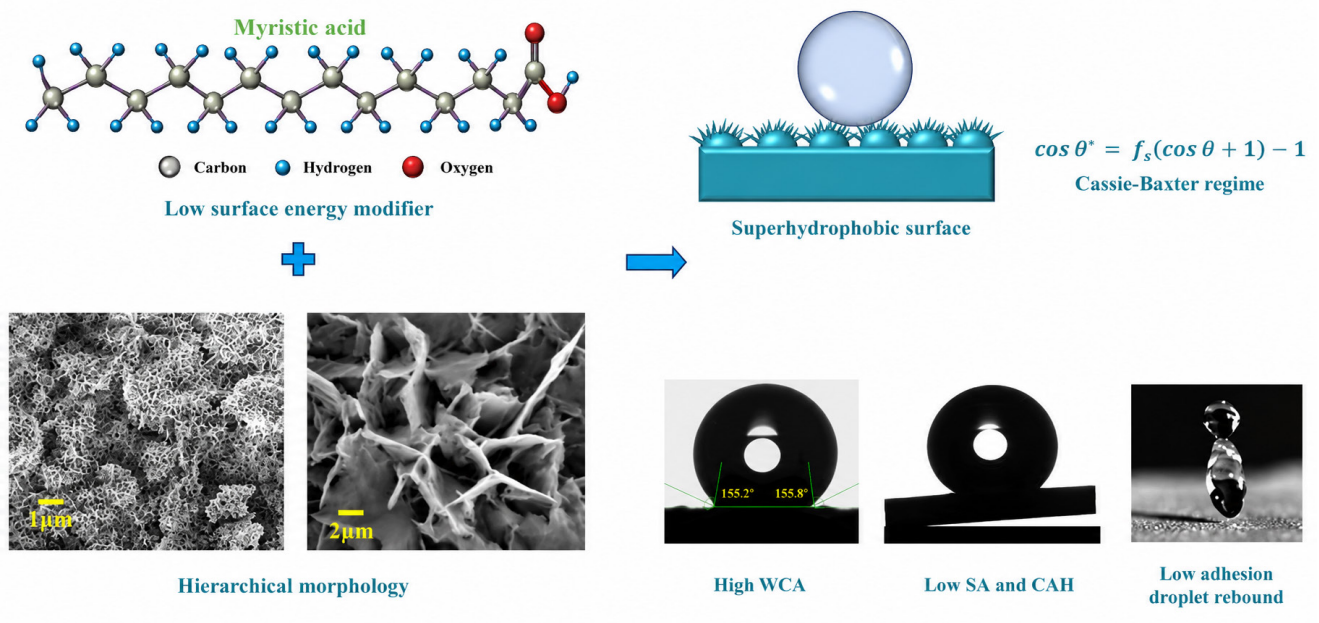

Fig. 3 Schematics of superhydrophobic surface formation and wetting behaviour. Hierarchical surface roughness generated by Zn deposition, combined with low surface energy modification by MTA, promotes a Cassie–Baxter wetting regime. The entrapped air pockets reduce the solid–liquid contact fraction (fs), as described by the Cassie–Baxter relation, leading to high contact angle, low hysteresis, and efficient droplet rebound.

2 Methodology

2.1 Sample and solution preparation

In this study, copper plates with a purity of 99% were used as substrates. The copper sheets, with a thickness of 2 mm, were cut into square samples of 10 mm × 10 mm. Prior to coating, the samples were mechanically polished using a polishing machine with silicon carbide abrasive papers with grit sizes ranging from 150 to 2000 to obtain a mirror-like surface finish. After polishing, the samples were ultrasonically cleaned in deionized water and ethanol to remove residual contaminants from the surface. Following the cleaning process, the samples were degreased in a sodium hydroxide solution and subsequently rinsed again using ultrasonic cleaning. To activate the surface and improve coating adhesion, the samples were etched in a ferric chloride solution prior to electrodeposition. For the electrodeposition process, an aqueous electrolyte solution containing zinc acetate was prepared using deionized water. Electrodeposition was carried out using a direct current (DC) power supply at 5 V for 20 min. After deposition, the coated samples were thoroughly rinsed with deionized water and ethanol and then allowed to dry under ambient conditions. The deposited samples were subsequently annealed at 120 °C for 60 min to stabilize the coating structure. Finally, the samples were immersed in an ethanolic solution of MTA for 5 min to modify the surface with a low surface energy layer, followed by air drying under ambient conditions.

2.2 Measurement and analysis

The chemical composition of the coating was characterized using energy-dispersive X-ray spectroscopy (EDS), X-ray diffraction (XRD), and Fourier transform infrared spectroscopy (FTIR). XRD patterns were recorded using a PANalytical X'Pert PRO X-ray diffractometer (PANalytical B.V., Netherlands) employing Cu Kα radiation (λ = 1.5406 Å) and performed at 45 kV and 40 mA. FTIR spectra were recorded using a PerkinElmer Spectrum Two FTIR spectrophotometer (PerkinElmer, UK) spectrometer over the wavenumber range of 4000–400 cm^{-1} at a spectral resolution of 4 cm^{-1}. Elemental composition was determined using an energy-dispersive X-ray spectroscopy (EDS) system attached to the SEM. The combined XRD, FTIR, and EDS analyses were employed to identify the crystalline phases, chemical functionalities, and elemental composition of the coating. Since the chemical composition of the surface governs its surface energy, these analyses are essential for understanding the wettability characteristics of the fabricated coating. The surface morphology and microstructural features of the coating were examined using a Zeiss Supra 40 VP (Carl Zeiss Microscopy GmbH, Germany) scanning electron microscope (SEM) operated at an accelerating voltage of 5 kV and a working distance of approximately 4.1 mm. SEM image analysis was performed using ImageJ (Version 1.54p; Wayne Rasband and contributors, National Institutes of Health, Bethesda, MD, USA).

For void fraction analysis, high-resolution SEM micrographs were first converted into 8-bit grayscale images using ImageJ, followed by controlled contrast enhancement through histogram normalization (0.3–0.5% saturated pixels) to improve phase discrimination between solid features and void regions. Where necessary, background correction was applied to minimize non-uniform image intensity. The processed images were subsequently subjected to thresholding to generate binary images, from which the void fraction was quantified using the ImageJ software's area-fraction measurement tools. Particle size distribution analysis of the surface micro-clusters was also performed using ImageJ from calibrated SEM micrographs. Therefore, a combined analysis of surface chemistry and morphology is necessary to understand the mechanisms responsible for the observed superhydrophobic behaviour. Surface morphology plays a critical role in determining the roughness characteristics of the coating, which significantly influence wetting behavior and the stabilization of different wetting regimes. Therefore, a combined analysis of surface chemistry and morphology is necessary to understand the mechanisms responsible for the observed superhydrophobic behavior. The wettability characteristics of the coated surface, including the WCA and CAH, were measured using a goniometer (Model 290, ramé-hart instrument co., USA). The SA was determined by gradually tilting the sample until the droplet began to move. The dynamic interaction between water droplets and the coated surface was investigated using a Photron FASTCAM Mini UX50 160K-M-4GB (Photron, USA) high-speed camera to analyze droplet impact and rebound behavior.

3 Results and discussion

3.1 Chemical nature of the coating

The chemical nature of the coating was analysed through FTIR, XRD and EDS of the coated sample (Fig. 4). The FTIR sharp absorption bands (Fig. 4(a)) at 723 cm^{-1} and 743 cm^{-1} are assigned to the $-CH_2$ rocking modes of long MTA chain, whereas the bands at 839 cm^{-1}, 902 cm^{-1} and 948 cm^{-1} are assigned to the out of plane C-H bending or wagging [34]. In the mid-region, the minor vibrational bands at 1043 cm^{-1}, 1094 cm^{-1}, 1192 cm^{-1}, and 1245 cm^{-1}

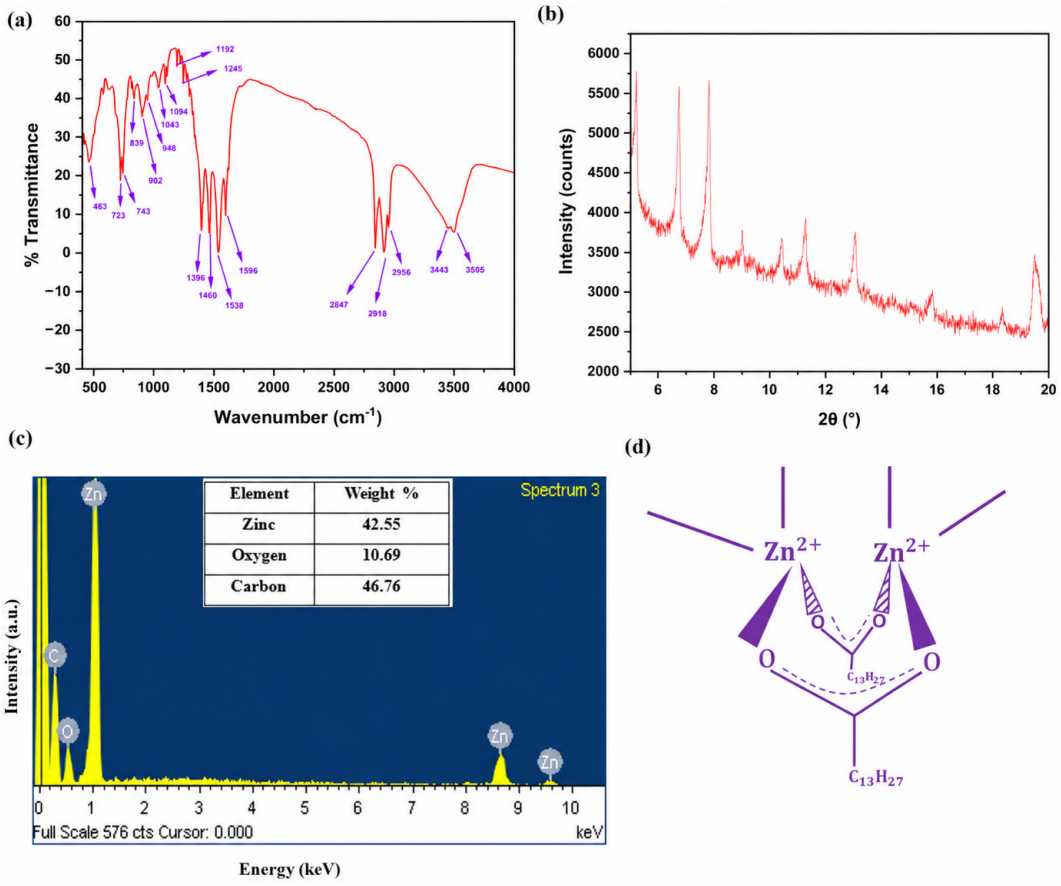

Fig. 4 Characterization of the coated surface: (a) FTIR spectrum showing characteristic peaks corresponding to ZnMTA formation; (b) XRD pattern of the coated sample indicating crystalline phases associated with the deposited layer; (c) EDS spectrum confirming the presence of Zn, O, and C elements on the coating; and (d) schematic representation of the bridging bidentate coordination structure of ZnMTA.

are attributed to C−O stretching, $-CH_2$ twisting and wagging. The prominent absorption bands located at 1396 cm^{-1} and 1538 cm^{-1} are attributed to the symmetric and asymmetric stretching vibrations of the carboxylate (COO^-) group, respectively. The appearance of these characteristic carboxylate bands, together with the absence of the C=O stretching absorption band in the 1700–1725 cm^{-1} region characteristic of free MTA, confirm the formation of ZnMTA on the surface. Furthermore, the separation between the asymmetric and symmetric COO^- stretching vibrations ($\Delta\nu \approx 142$ cm^{-1}) suggests a bridging bidentate coordination mode, wherein the carboxylate oxygen atoms interact with two different Zn^{2+} centres, resulting in the formation of an extended coordination network [35] (Fig. 4(d)). The vibrational band at 1460 cm^{-1} is attributed to the $-CH_2$ scissoring, due to the presence of a long-chain fatty acid. The other absorption band lie in the high wavenumber region where 2847 cm^{-1}, 2918 cm^{-1}, 2956 cm^{-1} is assigned to the C-H stretching from the CH_2 and CH_3 groups present in long alkyl chains of MTA [36]. The vibrational band at 3443 cm^{-1} may suggests adsorbed water or surface hydroxyl groups, and at 3505 cm^{-1} is due to weakly hydrogen bonded −OH groups. An absorbance band can also be observed in the region 400–600 cm^{-1} which is assigned to the stretching of Zn−O bond, which may be due to the formation of zinc oxide or ZnMTA or both. It may be possible that some of the zinc molecules may have converted into zinc oxide during the annealing stage. The XRD of the coated sample (Fig. 4(b)) shows peaks at 2θ values of 5.12°, 6.79°, 7.75°, 9.01°, 10.40°, 11.25°, 13.03° and 19.46°, where 2θ is the diffraction angle between the incident and diffracted X-ray beams. The peak at 5.12° is due to first-order lamellar spacing of ZnMTA which come out to be around 1.72 nm [37–39].

The ZnMTA usually form bilayer or multilayer structure due long fatty acid chain. The peak at 10.4° can be attributed to the distorted bilayer which reduced the overall layer spacing. The peaks observed in from XRD analysis is very similar to the ones found in metal soaps [37]. The presence of these peaks confirms the formation of ZnMTA on the copper substrate. EDS analysis (Fig. 4(c)) of the coated sample shows a high mass percentage of carbon and oxygen in addition to the zinc which can be attributed to the formation of long chain myristate salt. The chemical nature of the coating confirms a low surface energy MTA deposition on zinc coated copper leads to the formation of ZnMTA.

3.2 Surface morphology

The SEM images (Fig. 5(a)-(e)) provide valuable insights into the morphology of the coated surface at different magnifications. At lower magnification (Fig. 5(a)), the surface exhibits densely distributed spherical micro-clusters that uniformly cover the substrate, indicating the successful formation of a textured coating layer over the copper surface. These micro-scale clusters appear to be randomly distributed but closely packed, creating a rough topography that significantly increases the effective surface roughness. Such surface roughness plays an important role in enhancing the wetting properties of engineered surfaces. Another important feature observed in the SEM images is the presence of interconnected voids and gaps between the micro–clusters and nano–petal structures (Figs. 5(c) and 5(d)). These voids play a crucial role in determining the wetting behavior of the surface. When a water droplet comes into contact with the coated surface, these cavities act as air trapping sites that retain air beneath the droplet. The trapped air pockets effectively reduce the solid–liquid contact area, allowing the droplet to rest partially on the solid surface and partially on the entrapped air layer. This phenomenon corresponds to the Cassie–Baxter wetting regime, where the presence of air pockets within the surface structure leads to reduced droplet adhesion and enhanced water repellency. Consequently, droplets experience lower resistance while moving across the surface, which contributes to the observed low CAH and reduced SA. Therefore, the hierarchical micro–nano morphology consisting of micro-clusters, nano-petal structures, and interconnected voids is expected to play a crucial role in imparting superhydrophobic characteristics to the coated surface.

To further quantify the surface morphology, particle size distribution analysis of the micro-clusters was performed using the ImageJ software at a magnification of 10 μm (Fig. 5(f)). The analysis indicates that the micro-clusters possess an average diameter of 26.98 μm with a standard deviation of 7.97 μm, suggesting a relatively consistent microstructural distribution across the coating. The void fraction of the superhydrophobic surface was quantified via digital image analysis using ImageJ (Fig. 6) [40]. It should be noted that image-based void fraction estimation provides a two-dimensional projected representation of the surface morphology and does not fully capture subsurface features, pore depth, or other three-dimensional roughness characteristics. Furthermore, the calculated values may be influenced

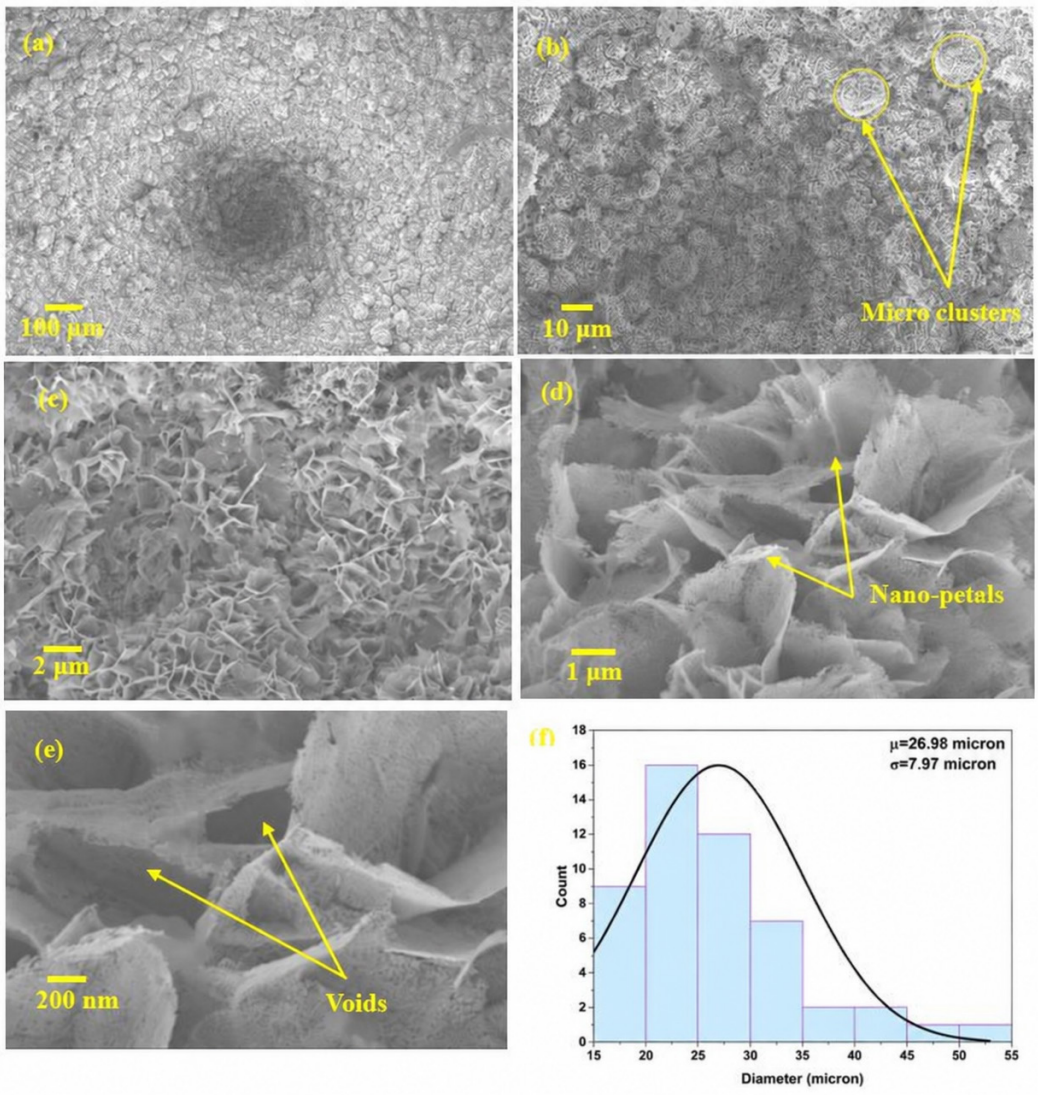

Fig. 5 SEM images of the coated copper surface at different magnifications illustrating the hierarchical micro–nano morphology responsible for the observed superhydrophobic behaviour: (a) low magnification image (100 µm scale) showing the distribution of micro-scale clusters over the surface; (b) intermediate magnification (10 µm scale) revealing densely packed micro-bumps; (c) higher magnification (2 µm scale) displaying interconnected nano-petal structures forming a rough network; (d) detailed view of the hierarchical architecture (1 µm scale) composed of micro-clusters decorated with nano-scale petals; (e) close-up image (200 nm scale) highlighting petal-like nanostructures and voids that can trap air pockets; (f) particle size distribution of the micro-clusters obtained using ImageJ analysis from the SEM image at 100 µm magnification.

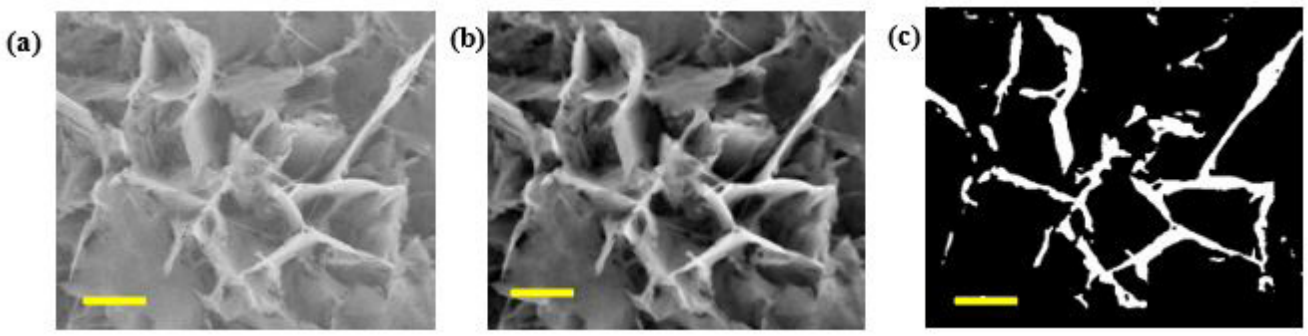

Fig. 6 Quantification of surface void fraction for Cassie–Baxter analysis. (a) SEM image of Zn-based superhydrophobic coating, (b) contrast-enhanced grayscale image, (c) binary image obtained *via* Otsu thresholding using ImageJ, where white regions denote solid structures and black regions represent air pockets. Scale bars are 250 nm.

by image resolution, threshold selection, and local surface heterogeneity. Nevertheless, this approach is widely employed for estimating the solid–air fractions governing apparent wettability and enables meaningful comparison of textured surfaces. High-resolution SEM micrographs were first converted into 8-bit grayscale images, followed by controlled contrast enhancement using histogram normalization (0.3–0.5% saturated pixels) to improve phase discrimination between solid features and void regions.

Background correction was optionally performed prior to segmentation to account for non-uniform illumination. Binary images were then generated using an automated global thresholding approach based on Otsu's method [41], which determines an optimal threshold by minimizing the intra-class variance between foreground and background pixel populations. The robustness of the segmentation was further verified using the Triangle thresholding method [42], which identifies the threshold from the geometric relationship between the histogram peak and the histogram tail. Post-thresholding, morphological operations were applied to eliminate isolated noise pixels and ensure the structural continuity of the segmented features.

The void fraction (f_v) was calculated as the ratio of the projected void area to the total image area, while the solid fraction (f_s) was obtained as ($1 - f_v$). To ensure statistical reliability, multiple regions of interest from different areas of the sample were analysed under identical processing parameters. The average void fraction was determined to be 0.867 ± 0.054, indicating a highly porous hierarchical surface capable of entrapping significant air pockets. Such a high void fraction is conducive to a Cassie–Baxter-type wetting regime and likely contributes to the observed superhydrophobic behaviour.

3.3 Wettability

To evaluate the wettability of the fabricated surfaces, the static WCA, CAH, and SA were measured. The variation in the contact angle with MTA concentration is presented in Fig. 7. The results demonstrate a nonlinear dependence of wettability on MTA concentration. Initially, the contact angle increases with increasing concentration, indicating enhanced hydrophobicity due to improved surface coverage and reduced surface energy. However, beyond an optimum concentration, a slight decrease in the contact angle was observed. The maximum performance was obtained at a concentration of 0.1 M MTA, yielding a contact angle of 156° ± 0.8°, a CAH of 5°, and a SA of 4°. These values indicate excellent water-repellent properties.

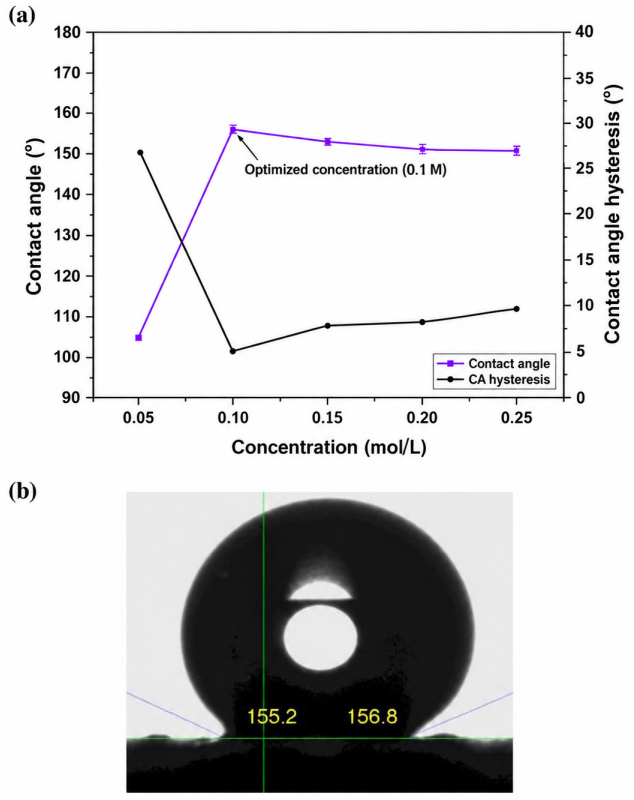

Fig. 7 (a) The variation of contact angle with the concentration of MTA, (b) the contact angle of a sessile drop on the coated surface

The observed variation in wettability is governed by the combined effects of surface chemistry and morphology. The increase in the contact angle with increasing MTA concentration up to 0.1 M can be attributed to the progressive reduction in the surface energy owing to the adsorption of long-chain fatty acid molecules. The increase in contact angle with increasing MTA concentration up to 0.1 M can be attributed to the progressive reduction in surface energy owing to the adsorption of long-chain fatty acid molecules. According to Young's equation [43], an increase in contact angle corresponds to a decrease in the solid–liquid interfacial energy (γ_{sl}) relative to the solid–vapor interfacial energy. The adsorption of ZnMTA exposes non-polar hydrocarbon chains at the surface, thereby weakening interactions with polar water molecules and reducing the tendency of water to spread on the surface. At higher concentrations, the slight decrease in the contact angle and increase in hysteresis can be attributed to the over-deposition of MTA, which may lead to the partial filling of surface features. This reduces the effective air fraction at the interface and promotes droplet pinning, thereby diminishing the superhydrophobic performance.

The optimized surface at 0.1 M MTA was further analyzed using the Cassie–Baxter model by incorporating the

void fraction obtained from SEM image analysis. The void fraction was determined to be 0.867 ± 0.05, corresponding to a solid fraction of 0.133. According to the Cassie–Baxter relation (Eq. (1)):

$$\cos\theta^* = f_s\left(\cos\theta + 1\right) - 1 \tag{1}$$

where θ* is the apparent contact angle on the textured surface, θ is the intrinsic contact angle of the chemically modified smooth surface, and f_s represents the solid–liquid contact fraction. For fatty-acid-modified metal oxide surfaces, the intrinsic contact angle is typically reported in the range of 95º to 100° [23]. By substituting f_s = 0.133 and θ = 95º to 100°, the predicted apparent contact angle (θ*) was estimated to lie in the range of 151.5° to 153°. This predicted range shows close agreement with the experimentally measured contact angle of 156°, indicating the validity of the Cassie–Baxter model in describing the wetting behavior of the fabricated surface.

A high void fraction indicates that a substantial portion of the droplet is supported by trapped air pockets within the hierarchical micro–nano structure, resulting in a composite solid–air and solid–liquid interface. This significantly reduces the effective solid–liquid contact area, thereby minimizing adhesion and promoting droplet mobility. Furthermore, the presence of interconnected voids enhances the stability of the Cassie–Baxter state by resisting liquid penetration into surface asperities under static conditions. Minor deviations between theoretical predictions and experimental values may arise from surface heterogeneity, local variations in roughness, and uncertainties associated with threshold-based image segmentation. Additionally, dynamic factors, such as contact line pinning and partial wetting transitions during droplet deposition, may also influence the measured contact angle. Nevertheless, the strong agreement between theoretical and experimental results confirms that the superior water repellency of the optimized surface originates from a stable Cassie–Baxter wetting regime governed by its high void fraction and hierarchical morphology.

The role of surface morphology is further supported by SEM observations, revealing the presence of hierarchical micro–nano structures and interconnected voids. These features are critical in reducing CAH and SA by minimizing contact line pinning. The trapped air pockets within the surface structure act as a barrier, allowing droplets to roll off easily under small tilt angles. However, at higher MTA concentrations, the increase in CAH and SA (Figs. 7(a) and 8(a)) suggests enhanced pinning, likely

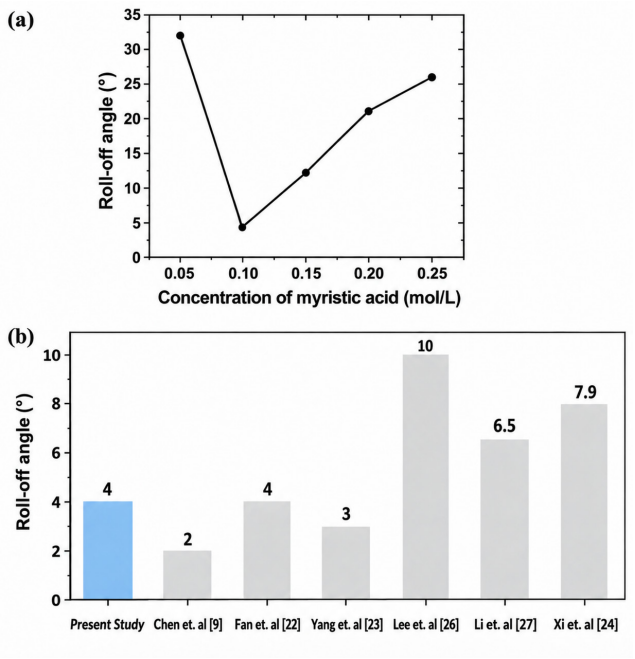

Fig. 8 (a) Variation of roll-off angle with MTA concentration showing minimum roll-off at 0.1 M. (b) Comparative roll-off angles of the present coating with previously reported superhydrophobic surfaces from literature [9, 22–24, 26, 27].

due to the partial loss of air pockets caused by excessive surface coverage. Fig. 8(b) compares the SA of the present study with reported values in the literature. The developed coating exhibits a SA of 4°, which is comparable to the best-performing surfaces and lower than several reported engineered surfaces. This demonstrates the effectiveness of the hierarchical structure and surface modification in achieving low adhesion and enhanced droplet mobility.

Although static and quasi-static parameters, such as the WCA, CAH, and SA, provide important insights into surface wettability, they do not fully capture the dynamic interaction between droplets and the textured surface. Superhydrophobic surfaces exhibiting low adhesion often demonstrate droplet rebound upon impact, which is commonly associated with a Cassie–Baxter-type wetting state. Therefore, to further investigate the dynamic wetting characteristics, droplet impact experiments were conducted using high-speed imaging. The results provide additional evidence of weak liquid–solid interactions and support the superhydrophobic nature of the developed coating.

3.4 Droplet impact and rebound behaviours

To further investigate the dynamic wetting behaviour of the hierarchical coating, droplet impact experiments were conducted by releasing water droplets onto the coated surface from a fixed height and recording the

subsequent impact dynamics using high-speed imaging at 4000 frames per second (fps) Fig. 9. presents sequential frames illustrating the evolution of the droplet during impact and rebound. Upon impact (t = 0 ms), the droplet spreads rapidly due to its kinetic energy, forming a thin liquid film on the surface at t = 2.5 ms. The droplet continues to expand radially until it reaches its maximum spreading diameter at approximately t = 6 ms.

To quantitatively characterize the observed spreading behaviour, the droplet impact dynamics were analysed using the Weber number (*We*), which represents the ratio of inertial forces to capillary forces associated with surface tension. Surface tension originates from cohesive intermolecular forces within the liquid and acts to minimize the liquid–air interfacial area.

$$We = \frac{\rho V^2 D}{\gamma} \tag{2}$$

where ρ is the liquid density, V is the impact velocity of the droplet, D is the droplet diameter, and γ is the surface tension of the liquid [44, 45]. The Weber number is widely used to characterize droplet impact dynamics and spreading behavior on solid surfaces, as it quantifies the relative importance of inertial and capillary effects. For Weber numbers greater than unity, inertial forces exceed capillary forces during the initial impact stage, promoting droplet spreading. For the droplet used in the present study (diameter = 1.7 mm and release height = 50 mm), the Weber number was estimated to be approximately $We \approx 23$. At the calculated Weber number of approximately 23 [46, 47], the droplet underwent significant spreading while maintaining its integrity throughout the impact event. Nevertheless, the droplet remained highly mobile and did not exhibit significant contact-line pinning during retraction. During spreading, the droplet's kinetic energy is stored as surface energy through the creation of additional liquid–air interfacial area. As the droplet retracts, a significant fraction of this stored energy is recovered and transformed back into kinetic energy, enabling droplet lift-off and rebound. The observed energy recovery, indicates minimal energy

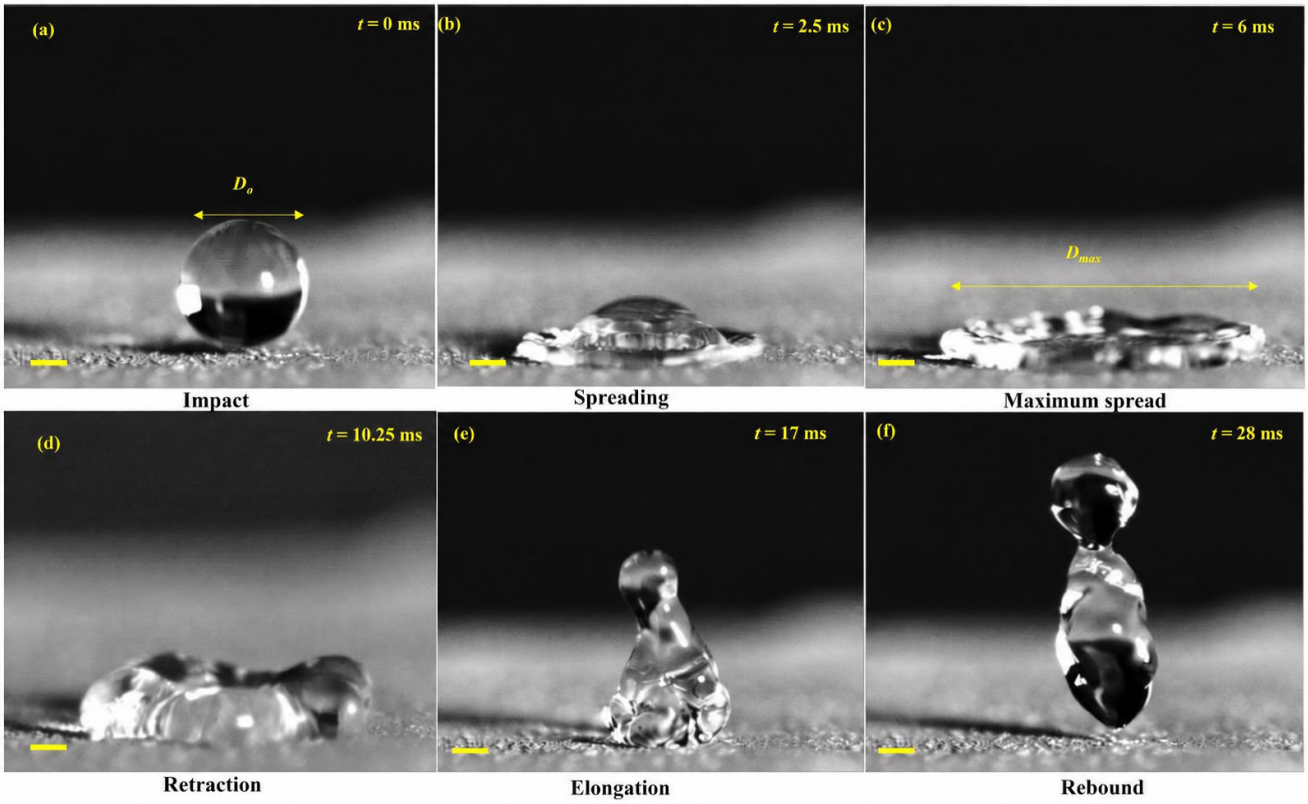

Fig. 9 High-speed image sequence illustrating the impact dynamics of a water droplet on the coated surface: (a) droplet impact (t = 0 ms); (b) spreading stage (t = 2.5 ms); (c) maximum spreading diameter (t = 6 ms); (d) early stage of retraction driven by surface tension; (e) final stage of retraction just before droplet detachment (t = 17 ms); and (f) droplet rebound from the surface (t = 28 ms). The initial droplet diameter (D_0) and maximum spreading diameter (D_{max}) are indicated in panels (a) and (c), respectively, and were used to calculate the maximum spreading factor. The observed droplet rebound and short contact time indicate weak liquid–solid adhesion and confirm the superhydrophobic nature of the coated surface. Scale bar is 0.5 mm.

dissipation through liquid–solid adhesion. Consequently, complete rebound was achieved despite significant deformation during impact. Such behaviour provides further evidence for a stable Cassie–Baxter wetting state, wherein the high surface void fraction (0.867 ± 0.054) promotes air entrapment, reduces effective solid–liquid contact, and suppresses contact-line pinning during retraction phase.

Using the empirical scaling relation $\beta = We^{1/4}$ [48], the predicted spreading factor is $\beta_{max} = 2.2$, which is in good agreement with the experimentally measured value. To further validate the observed droplet impact dynamics, the temporal evolution of the spreading factor was compared with literature data reported by Rioboo et al. [47], using dimensionless time scaling, $t^* = tV/D_o$ (where t is time, V is impact velocity and D_o is the initial droplet diameter). As shown in Fig. 10, both datasets exhibit a similar trend characterized by rapid inertia-driven spreading, followed by capillary-driven retraction. The slight difference in the maximum spreading factor between the present study ($\beta_{max} = 2.33$) and that reported by Rioboo et al. ($\beta_{max} = 2.6$) may arise from differences in the impact conditions (higher Weber number of 52 in case if Rioboo et al.) and fluid properties employed in the two studies. The difference in the maximum spreading factor between the present study ($\beta_{max} = 2.33$) and the literature ($\beta_{max} = 2.6$) can be attributed to the lower Weber number ($We = 23$) compared to that of Rioboo et al. ($We = 52$), indicating reduced inertial effects. Overall, the agreement in the spreading–retraction behaviour suggests that the droplet impact dynamics in the present study are consistent with classical inertial–capillary scaling.

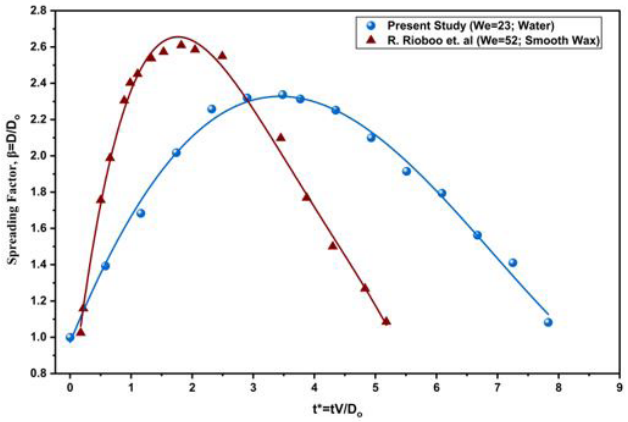

Fig. 10 Comparison of the temporal evolution of the spreading factor ($\beta = D/D_0$) as a function of dimensionless time ($t^* = tV/D_0$) for the present study ($We \approx 23$) and literature data from Rioboo et al. ($We \approx 52$, smooth wax surface) [47]. Both datasets exhibit a similar trend characterized by inertia-driven spreading followed by capillary-driven retraction. The higher maximum spreading factor observed for Rioboo et al. [47] is attributed to the higher Weber number, indicating stronger inertial effects.

4 Conclusion

A superhydrophobic coating was successfully fabricated on copper substrates through electrochemical deposition, followed by annealing and surface modification with MTA. Scanning electron microscopy revealed a hierarchical surface morphology consisting of nano-petal structures superimposed on micro-scale clusters. This binary roughness generates numerous void spaces capable of trapping air, which is essential for achieving superhydrophobic behavior. Quantitative image analysis further indicated an average void fraction of approximately 86.7 ± 5.4%, suggesting the presence of significant air pockets within the hierarchical structure, which is conducive to a Cassie–Baxter-type wetting regime. Chemical characterization using FTIR, XRD, and EDS confirmed the formation of ZnMTA, resulting from the interaction between zinc species and long-chain MTA molecules, thereby imparting a low-surface-energy layer to the surface. As a result of the combined effects of hierarchical roughness and low surface energy, the coating exhibited excellent water repellency, with a WCA of 156° ± 0.8°, CAH of 5°, and a spreading factor of approximately 2.33. High-speed imaging further demonstrated droplet rebound with a contact time of 28 ms, indicating weak liquid–solid adhesion and confirming the presence of a Cassie–Baxter wetting regime. The developed coating therefore demonstrates strong potential for applications such as anti-corrosion protection, anti-icing surfaces, and self-cleaning coatings. Moreover, the simplicity of the fabrication process and the use of readily available materials make this approach promising for practical and scalable industrial applications. Future work should focus on evaluating the long-term durability and stability of the coating under realistic service conditions, including mechanical abrasion, environmental exposure, and extended corrosion testing, to further assess its suitability for industrial deployment.

Acknowledgement

The authors gratefully acknowledge the Department of Mechanical Engineering, NIT Agartala; the Central Instrumentation Centre, Tripura University; and the Center for Nano Science (CNS) Facility, IIT Kanpur, for providing the research and characterization facilities used in this work.

References

[1] Li, J., Liu, X., Ye, Y., Zhou, H., Chen, J. "A simple solution-immersion process for the fabrication of superhydrophobic cupric stearate surface with easy repairable property", Applied Surface Science, 258(5), pp. 1772–1775, 2011. https://doi.org/10.1016/j.apsusc.2011.10.042

[2] Huang, Y., Sarkar, D. K., Gallant, D., Chen, X. G. "Corrosion resistance properties of superhydrophobic copper surfaces fabricated by one-step electrochemical modification process", Applied Surface Science, 282, pp. 689–694, 2013. https://doi.org/10.1016/j.apsusc.2013.06.034

[3] Tam, J., Palumbo, G., Erb, U. "Recent Advances in Superhydrophobic Electrodeposits", Materials, 9(3), 151, 2016. https://doi.org/10.3390/ma9030151

[4] Ejenstam, L., Ovaskainen, L., Rodriguez-Meizoso, I., Wågberg, L., Pan, J., Swerin, A., Claesson, P. M. "The effect of superhydrophobic wetting state on corrosion protection - The AKD example", Journal of Colloid Interface Science, 412, pp. 56–64, 2013. https://doi.org/10.1016/j.jcis.2013.09.006

[5] Wang, Y., Cai, W., Zhang, Y., Ji, J., Zheng, H., Yan, D., Liu, X. " Superhydrophobic wearable sensor: fabrication, application, and perspective", Discover Nano, 19(1), 176, 2024. https://doi.org/10.1186/s11671-024-04138-x

[6] Guo, Z. G., Fang, J., Hao, J. C., Liang, Y. M., Liu, W. M. "A novel approach to stable superhydrophobic surfaces", ChemPhysChem, 7(8), pp. 1674–1677, 2006. https://doi.org/10.1002/cphc.200600217

[7] Ensikat, H. J., Ditsche-Kuru, P., Neinhuis, C., Barthlott, W. "Superhydrophobicity in perfection: The outstanding properties of the lotus leaf", Beilstein Journal of Nanotechnology, 2, pp. 152–161, 2011. https://doi.org/10.3762/bjnano.2.19

[8] Bhushan, B., Jung, Y. C., Koch, K. "Micro-, nano- And hierarchical structures for superhydrophobicity, self-cleaning and low adhesion", Philosophical Transactions of the Royal Society A: Mathematical, Physical and Engineering Sciences, 367(1894), pp. 1631–1672, 2009. https://doi.org/10.1098/rsta.2009.0014

[9] Chen, Z., Hao, L., Chen, C. "A fast electrodeposition method for fabrication of lanthanum superhydrophobic surface with hierarchical micro-nanostructures", Colloids and Surfaces A: Physicochemical and Engineering Aspects, 401, pp. 1–7, 2012. https://doi.org/10.1016/j.colsurfa.2012.02.020

[10] Wenzel, R. N. "Resistance of solid surfaces to wetting by water", Industrial & Engineering Chemistry, 28(8), pp. 988–994, 1936. https://doi.org/10.1021/ie50320a024

[11] Cassie, A. B. D., Baxter, S. "Wettability of porous surfaces", Transactions of the Faraday Society, 40, pp. 546–551, 1944.

[12] Chakraborty, M., Weibel, J. A., Schaber, J. A., Garimella, S. V. "The Wetting State of Water on a Rose Petal", Advanced Materials Interfaces, 6(17), 1900652, 2019.

[13] Bhushan, B., Nosonovsky, M. "Rose Petal Effect", In: Bhushan, B. (ed.) Encyclopedia of Nanotechnology, Springer: Dordrecht, 2012, pp. 2265–2272. ISBN 978-90-481-9751-4 https://doi.org/10.1007/978-90-481-9751-4_157

[14] Parvate, S., Dixit, P., Chattopadhyay, S. "Superhydrophobic Surfaces: Insights from Theory and Experiment", The Journal of Physical Chemistry B, 124(8), pp. 1323–1360, 2020. https://doi.org/10.1021/acs.jpcb.9b08567

[15] Wang, B., Zhang, Y., Shi, L., Li, J., Guo, Z. "Advances in the theory of superhydrophobic surfaces", Journal of Materials Chemistry, 22(38), pp. 20112–20127, 2012. https://doi.org/10.1039/c2jm32780e

[16] Hooda, A., Goyat, M. S., Pandey, J. K., Kumar, A., Gupta, R. "A review on fundamentals, constraints and fabrication techniques of superhydrophobic coatings", Progress in Organic Coatings, 142, 105557, 2020. https://doi.org/10.1016/j.porgcoat.2020.105557

[17] Zhang, D., Wang, L., Qian, H., Li, X. "Superhydrophobic surfaces for corrosion protection: a review of recent progresses and future directions", Journal of Coatings Technology Research, 13(1), pp. 11–29, 2016. https://doi.org/10.1007/s11998-015-9744-6

[18] Wang, S., Liu, K., Yao, X., Jiang, L. "Bioinspired surfaces with superwettability: New insight on theory, design, and applications", Chemical Reviews, 115(16), pp. 8230–8293, 2015. https://doi.org/10.1021/cr400083y

[19] Fan, Y., Chen, Z., Liang, J., Wang, Y., Chen, H. "Preparation of superhydrophobic films on copper substrate for corrosion protection", Surface and Coatings Technology, 244, pp. 1–8, 2014. https://doi.org/10.1016/j.surfcoat.2014.01.005

[20] Liu, Y., Li, S., Zhang, J., Wang, Y., Han, Z., Ren, L. "Fabrication of biomimetic superhydrophobic surface with controlled adhesion by electrodeposition", Chemical Engineering Journal, 248, pp. 440–447, 2014. https://doi.org/10.1016/j.cej.2014.03.046

[21] Yuan, S., Pehkonen, S. O., Liang, B., Ting, Y. P., Neoh, K. G., Kang, E. T. "Superhydrophobic fluoropolymer-modified copper surface via surface graft polymerisation for corrosion protection", Corrosion Science, 53(9), pp. 2738–2747, 2011. https://doi.org/10.1016/j.corsci.2011.05.008

[22] Fan, Q., Ji, X., Lan, Q., Zhang, H., Li, Q., Zhang, S., Yang, B. "An anti-icing copper-based superhydrophobic layer prepared by one-step electrodeposition in both cathode and anode", Colloids and Surfaces A: Physicochemical and Engineering Aspects, 637, 128220, 2022. https://doi.org/10.1016/j.colsurfa.2021.128220

[23] Yang, Z., Liu, X., Tian, Y. "Fabrication of super-hydrophobic nickel film on copper substrate with improved corrosion inhibition by electrodeposition process", Colloids and Surfaces A: Physicochemical and Engineering Aspects, 560, pp. 205–212, 2019. https://doi.org/10.1016/j.colsurfa.2018.10.024

[24] Xi, W., Qiao, Z., Zhu, C., Jia, A., Li, M. "The preparation of lotus-like super-hydrophobic copper surfaces by electroplating", Applied Surface Science, 255(9), pp. 4836–4839, 2009. https://doi.org/10.1016/j.apsusc.2008.12.012

[25] Jie, H., Xu, Q., Wei, L., Min, Y. L. "Etching and heating treatment combined approach for superhydrophobic surface on brass substrates and the consequent corrosion resistance", Corrosion Science, 102, pp. 251–258, 2016. https://doi.org/10.1016/j.corsci.2015.10.013

[26] Lee, J. M., Bae, K. M., Jung, K. K., Jeong, J. H., Ko, J. S. "Creation of microstructured surfaces using Cu–Ni composite electrodeposition and their application to superhydrophobic surfaces", Applied Surface Science, 289, pp. 14–20, 2014. https://doi.org/10.1016/j.apsusc.2013.10.066

[27] Li, H., Yu, S., Hu, J., Yin, X. "Modifier-free fabrication of durable superhydrophobic electrodeposited Cu-Zn coating on steel substrate with self-cleaning, anti-corrosion and anti- scaling properties", Applied Surface Science, 481, pp. 872–882, 2019. https://doi.org/10.1016/j.apsusc.2019.03.123

[28] Mamgain, H. P., Brajpuriya, R., Pati, P. R., Pandey, J. K. "Fabrication of bio-mimetic low surface energy modified copper- aluminum based superhydrophobic coating enhancing anti-corrosion efficiency of metal by electro-assisted deposition", Materialwiss. Werkstofftech, 57(1), pp. 42–48, 2026. https://doi.org/10.1002/mawe.70077

[29] Tran, N. G., Chun, D. M., Abd-Elrahim, A. G. "Superhydrophobic aluminum surfaces with nano-micro hierarchical composite structures: A novel and sustainable approach to corrosion protection", Journal of Alloys and Compounds, 960, 170907, 2023. https://doi.org/10.1016/j.jallcom.2023.170907

[30] Wang, T., Guo, Q., Zhang, T. C., Zhang, Y. X., Yuan, S. "Large-scale prepared superhydrophobic HDTMS-modified diatomite/epoxy resin composite coatings for high-performance corrosion protection of magnesium alloys", Progress in Organic Coatings, 170, 106999, 2022. https://doi.org/10.1016/j.porgcoat.2022.106999

[31] Tan, H., Yin, H., Zhong, Y., Luo, Y., Lan, B., Li, T., Hu, C. "Fabrication of superhydrophobic Co/Ag composite coating via one-step electrodeposition for enhanced corrosion resistance and anti-biofouling performances", Colloids and Surfaces A: Physicochemical and Engineering Aspects, 707, 135926, 2025. https://doi.org/10.1016/j.colsurfa.2024.135926

[32] Extrand, C. W., Kumagai, Y. "An Experimental Study of Contact Angle Hysteresis", 191(2), pp. 378–383, 1997. https://doi.org/10.1006/jcis.1997.4935

[33] Tadmor, R. "Line energy and the relation between advancing, receding, and Young contact angles", Langmuir, 20(18), pp. 7659–7664, 2004. https://doi.org/10.1021/la049410h

[34] Pavia, D. L., Lampman, G. M., Kriz, G. S., Vyvyan, J. A. "Introduction to Spectroscopy", Cengage Learning, 2014. ISBN 9781305177826

[35] Deacon, G. B., Phillips, R. J. "Relationships between the carbon-oxygen stretching frequencies of carboxylato complexes and the type of carboxylate coordination", Coordination Chemistry Reviews, 33(3), pp. 227–250, 1980. https://doi.org/10.1016/S0010-8545(00)80455-5

[36] Silverstein, R. M., Webster, F. X., Kiemle, D. J., Bryce, D. L. "Spectrometric Identification of Organic Compounds", John Wiley & Sons, 2014. ISBN 978-0-470-61637-6

[37] Corbeil, M.-C., Robinet, L. "X-ray powder diffraction data for selected metal soaps", Powder Diffraction, 17(1), pp. 52–60, 2002. https://doi.org/10.1154/1.1431950

[38] Zhang, W., Ding, S., Zhuang, W., Wu, D., Liu, P., …, Sun, X. "InP/ZnS/ZnS Core/Shell Blue Quantum Dots for Efficient Light-Emitting Diodes", Advanced Functional Materials, 30(49), 2005303, 2020. https://doi.org/10.1002/adfm.202005303

[39] Sawada, K., Konaka, M. "Characterization of Fine Metallic Soap Particles by X-Ray Diffraction, Differential Scanning Calorimetry, and Specific Surface Area Analysis", Journal of Oleo Science, 53(12), pp. 627–640, 2004. https://doi.org/10.5650/jos.53.627

[40] Schindelin, J., Arganda-Carreras, I., Frise, E., Kaynig, V., Longair, M., …, Cardona, A. "Fiji: An open-source platform for biological-image analysis", Nature Methods, 9(7), pp. 676–682, 2012. https://doi.org/10.1038/nmeth.2019

[41] Otsu, N. "A threshold selection method from gray-level histograms", IEEE Transactions on Systems, Man, and Cybernetics, 9(1), pp. 62–66, 1979. https://doi.org/10.1109/TSMC.1979.4310076

[42] Zack, G. W., Rogers, W. E., Latt, S. A. "Automatic measurement of sister chromatid exchange frequency", Journal of Histochemistry & Cytochemistry, 25(7), pp. 741–753, 1977. https://doi.org/10.1177/25.7.70454

[43] Young, T. "An essay on the cohesion of fluids", Abstracts of the Papers Printed in the Philosophical Transactions of the Royal Society of London, 1832(1), pp. 171–172, 1832. https://doi.org/10.1098/rspl.1800.0095

[44] Može, M., Shang, Y., Jereb, S., Kovač, N., Štucin, M., Štrus, T., Rodič, P., Zupančič, M., Vetrano, M. R., Golobič, I. "Surface morphology effects on droplet spreading and rebound dynamics on subcooled superhydrophobic surfaces", Scientific Reports, 15(1), 29530, 2025. https://doi.org/10.1038/s41598-025-14634-4

[45] Richard, D., Clanet, C., Quéré, D. "Contact time of a bouncing drop", Nature 417(6891), p. 811, 2002. https://doi.org/10.1038/417811a

[46] Chowdhury, R., Mainul Hoque, M., Evans, G., Honeyands, T., Monaghan, B. J., Scimone, D., Mitra, S. "Impact dynamics and solidification behaviour of a molten droplet on a flat surface at different Weber numbers", Experimental Thermal and Fluid Science, 154, 111156, 2024. https://doi.org/10.1016/j.expthermflusci.2024.111156

[47] Rioboo, R., Marengo, M., Tropea, C. "Time evolution of liquid drop impact onto solid, dry surfaces", Experiments in Fluids, 33(1), pp. 112–124, 2002. https://doi.org/10.1007/s00348-002-0431-x

[48] Josserand, C., Thoroddsen, S. T. "Drop Impact on a Solid Surface", Annual Review of Fluid Mechanics, 48, pp. 365–391, 2016. https://doi.org/10.1146/annurev-fluid-122414-034401